This is a repository copy of *Influence of Oil and Gas Emissions on Summertime Ozone in the Colorado Northern Front Range*.

White Rose Research Online URL for this paper:
https://eprints.whiterose.ac.uk/103000/

Version: Published Version

RESEARCH ARTICLE

Key Points:
- Modeled photochemical O_3 production is NO_x-sensitive at a central location in the Colorado Northern Front Range
- Oil and natural gas VOC emissions contribute over 80% to the observed carbon mixing ratio and 17.4% to maximum modeled photochemical O_3
- Observed O_3 production efficiencies are variable but show an influence of less than 1.8 ppbv/ppbv from oil and natural gas VOC emissions

Supporting Information:
- Supporting Information S1

Correspondence to:
S. S. Brown,
steven.s.brown@noaa.gov

Influence of oil and gas emissions on summertime ozone in the Colorado Northern Front Range

Erin E. McDuffie[1,2,3], Peter M. Edwards[4], Jessica B. Gilman[2], Brian M. Lerner[1,2], William P. Dubé[1,2], Michael Trainer[2], Daniel E. Wolfe[1,5], Wayne M. Angevine[1,2], Joost deGouw[2,3], Eric J. Williams[2], Alex G. Tevlin[6], Jennifer G. Murphy[6], Emily V. Fischer[7], Stuart McKeen[1,2], Thomas B. Ryerson[2], Jeff Peischl[1,2], John S. Holloway[1,2], Kenneth Aikin[1,2], Andrew O. Langford[2], Christoph J. Senff[1,2], Raul J. Alvarez II[2], Samuel R. Hall[8], Kirk Ullmann[8], Kathy O. Lantz[1,9], and Steven S. Brown[2,3]

[1]Cooperative Institute for Research in Environmental Sciences, University of Colorado Boulder, Boulder, Colorado, USA, [2]Chemical Sciences Division, Earth System Research Laboratory, NOAA, Boulder, Colorado, USA, [3]Department of Chemistry, University of Colorado Boulder, Boulder, Colorado, USA, [4]Department of Chemistry, University of York, York, UK, [5]Physical Sciences Division, Earth System Research Laboratory, NOAA, Boulder, Colorado, USA, [6]Department of Chemistry, University of Toronto, Toronto, Ontario, Canada, [7]Department of Atmospheric Science, Colorado State University, Fort Collins, Colorado, USA, [8]Atmospheric Chemistry Observations and Modeling Laboratory, NCAR, Boulder, Colorado, USA, [9]Global Monitoring Division, Earth System Research Laboratory, NOAA, Boulder, Colorado, USA

Abstract Tropospheric O_3 has been decreasing across much of the eastern U.S. but has remained steady or even increased in some western regions. Recent increases in VOC and NO_x emissions associated with the production of oil and natural gas (O&NG) may contribute to this trend in some areas. The Northern Front Range of Colorado has regularly exceeded O_3 air quality standards during summertime in recent years. This region has VOC emissions from a rapidly developing O&NG basin and low concentrations of biogenic VOC in close proximity to urban-Denver NO_x emissions. Here VOC OH reactivity (OHR), O_3 production efficiency (OPE), and an observationally constrained box model are used to quantify the influence of O&NG emissions on regional summertime O_3 production. Analyses are based on measurements acquired over two summers at a central location within the Northern Front Range that lies between major regional O&NG and urban emission sectors. Observational analyses suggest that mixing obscures any OPE differences in air primarily influenced by O&NG or urban emission sector. The box model confirms relatively modest OPE differences that are within the uncertainties of the field observations. Box model results also indicate that maximum O_3 at the measurement location is sensitive to changes in NO_x mixing ratio but also responsive to O&NG VOC reductions. Combined, these analyses show that O&NG alkanes contribute over 80% to the observed carbon mixing ratio, roughly 50% to the regional VOC OHR, and approximately 20% to regional photochemical O_3 production.

1. Introduction

Tropospheric ozone (O_3) is a secondary pollutant that contributes to the degradation of regional air quality. The only known sources of tropospheric O_3 are through the intrusion of O_3-rich stratospheric air [*Roelofs and Lelieveld*, 1995] and the oxidation of volatile organic compounds (VOCs) in the presence of nitrogen oxides ($NO_x = NO + NO_2$) [*Chameides*, 1978; *Crutzen*, 1970]. In the past two decades, summertime maximum O_3 at rural (receptor) sites across much of the U.S. has exhibited a strongly decreasing trend [*Cooper et al.*, 2012], likely in response to concurrent, declining NO_x emissions [e.g., *Butler et al.*, 2011; *Cooper et al.*, 2012; *Environmental Protection Agency*, 2016]. Decreasing O_3 trends have been most pronounced in the eastern U.S., but generally more moderate, or even increasing, at high-elevation western sites [*Cooper et al.*, 2012]. Proposed explanations for upward trends include increases in summer temperatures, contributions from stratospheric intrusions, long-range transport of emissions from Asia, western wildfire activity, and/or regional oil and natural gas (O&NG) emissions [*Cooper et al.*, 2012, 2015]. Here we focus on summertime O_3 production impacted by O&NG activity in the Colorado Northern Front Range (NFR) (Figure 1), a region out of compliance with National Ambient Air Quality Standards (NAAQS) of 75 ppbv for O_3 since 2007 and expected to remain so under recently revised 2015 standards of 70 ppbv [*Colorado Department of Public Health and Environment (CDPHE)*, 2016].

The NFR (Figure 1) has urban O_3 precursor emissions in close proximity to those from other sectors, principally agriculture (e.g., animal feedlots) and O&NG production. The NFR's Wattenberg Gas Field of the greater Denver-Julesburg Basin has seen significant recent increases in O&NG production, with the number of active
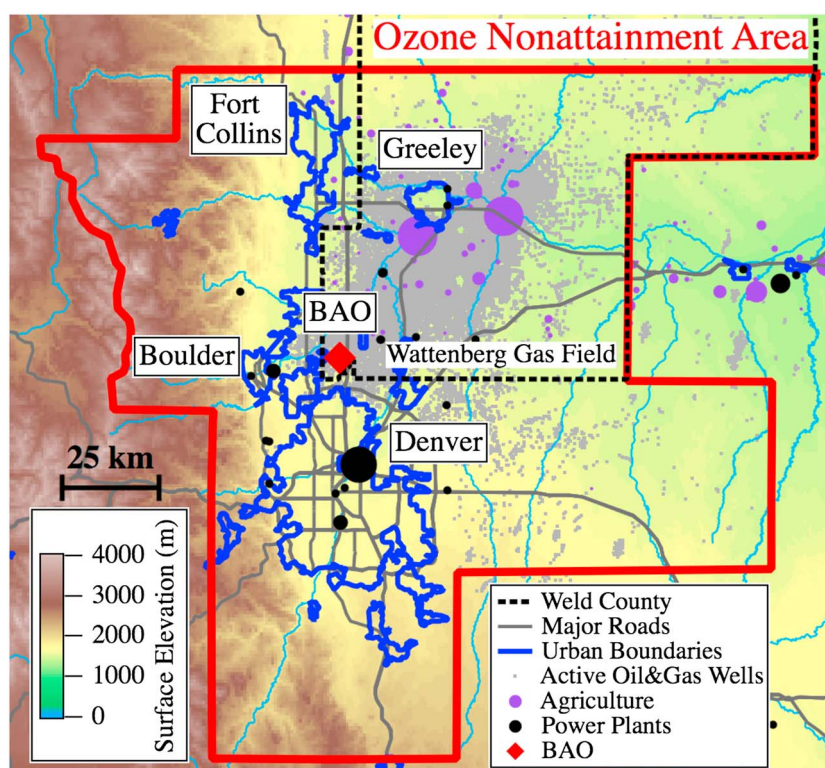
Figure 1. Elevation map of the Northern Front Range (NFR) region of Colorado showing the O_3 nonattainment area, Weld County (dashed lines), major roads, rivers, urban regions, power plants (scaled by relative NO_x emissions), large agricultural facilities (feedlots sized by animal capacity), and active O&NG wells [*Colorado Oil and Gas Conservation Commission (COGCC)*, 1/2016]. The red diamond indicates the location of the BAO measurement site.

wells nearly doubling in Weld County between January 2008 and July 2015 to over 27,000 [*Colorado Oil and Gas Conservation Commission (COGCC)*, 2/2016]. Though O&NG production has increased in multiple U.S. basins, a relatively small number of these basins lie in close proximity to large urban areas, as is the case with the Denver-Julesburg. Biogenic VOC mixing ratios (e.g., isoprene) are relatively low in the NFR compared to other U.S. O&NG producing regions, such as Texas and Pennsylvania [*Rutter et al.*, 2015; *Swarthout et al.*, 2015]. Lower biogenic mixing ratios may magnify the influence of O&NG emissions on regional O_3 production. Multiple studies have extensively characterized NFR VOC emissions, including those from O&NG activity [e.g., *Brantley et al.*, 2015; *Gilman et al.*, 2013; *Pétron et al.*, 2012, 2014; *Swarthout et al.*, 2013], but remain limited in terms of characterizing their influence on summertime O_3 production.

To date, relatively few studies have specifically assessed the influence of emissions associated with O&NG activity on regional summertime O_3 production. Several recent papers have focused on wintertime O_3 in O&NG producing regions in both the Upper Green River Basin of Wyoming [*Field et al.*, 2015; *Oltmans et al.*, 2014; *Rappenglück et al.*, 2014; *Schnell et al.*, 2009] and the Uintah Basin in Utah [*Ahmadov et al.*, 2015; *Carter and Seinfeld*, 2012; *Edwards et al.*, 2014, 2013; *Helmig et al.*, 2014; *Oltmans et al.*, 2014]. Winter O_3, however, is distinct from summertime urban-influenced O_3 and has so far only occurred in remote areas with low population densities and urban emissions. Winter O_3 is also specific to highly stable inversion conditions that cause an accumulation of VOC emissions from O&NG activity. The influence of O&NG emissions on summer O_3 near urban areas is not well characterized and is a potentially complex issue arising from the interaction of a variety of emissions.

Previous summertime O_3 analyses include two initial studies that used regional models to determine that O_3 production was positively influenced by emissions associated with O&NG activity in the Haynesville region in Texas [*Kemball-Cook et al.*, 2010] and across multiple western U.S. locations [*Rodriguez et al.*, 2009]. More recent work has suggested that O&NG-associated NO_x emissions, relative to those of VOCs, contribute disproportionally to summertime O_3 production. For example, O&NG-associated VOC emissions only contribute 8%

to O_3 precursors in California's San Joaquin Valley [*Gentner et al.*, 2014] and less than 20% and 7%, respectively, to the O_3 forming potential in the Barnett Basin near Fort Worth, Texas [*Rutter et al.*, 2015] and Pennsylvania's Marcellus Basin [*Swarthout et al.*, 2015]. Similarly, regional modeling of the Eagle Ford Basin in Texas showed that changes in regional summertime O_3 concentrations were not driven by O&NG-associated VOCs but rather by emissions of NO_x [*Pacsi et al.*, 2015]. As observed from space, NO_x levels associated with O&NG activity (e.g., flaring and combustion from O&NG extraction machinery and transport vehicles) have recently increased over three O&NG producing regions in the central U.S. [*Duncan et al.*, 2016]. In other states such as Pennsylvania, the influence of O&NG activity on O_3 may be underestimated or obscured due to (1) NO_x trends masked by surrounding urban emission reductions [*Duncan et al.*, 2016] and/or (2) gaps in the monitoring network for Environmental Protection Agency (EPA) criteria pollutants, such as NO_2 [*Carlton et al.*, 2014].

Here we apply three methods to characterize the influence of VOC and/or NO_x emissions on O_3 production in the NFR. These include VOC OH reactivity (OHR), O_3 production efficiency (OPE), and photochemical box modeling. The VOC OH reactivity (OHR) [e.g., *Gilman et al.*, 2013] is a measure of the kinetic oxidation of VOCs by the OH radical and is often the rate limiting step in photochemical O_3 production. A number of O&NG-focused studies have used this metric to highlight the potential contribution of O&NG VOCs to O_3 production in both summer and winter months [*Field et al.*, 2015; *Gilman et al.*, 2013; *Rutter et al.*, 2015; *Swarthout et al.*, 2013, 2015]. Although VOC OHR provides a simple assessment of the relative contribution of different VOCs to potential O_3 production, it does not incorporate information about radical propagation or its NO_x dependence, both of which are important for predicting the efficiency of O_3 production. Ozone production efficiency (OPE) [e.g., *Trainer et al.*, 1993] is a measure of the number of O_3 molecules produced, or number of NO_x interconversion cycles completed, before NO_x is lost through termination reactions (e.g., nitric acid (HNO_3) or organic nitrate production). The OPE is defined as the slope of odd oxygen ($O_x = NO_2 + O_3$) plotted against NO_z ($NO_z = NO_y - NO_x$, where NO_y is total oxidized reactive nitrogen). OPE analyses have been used to characterize urban and rural regions across the U.S. as documented in Table 1 of *Griffin et al.* [2004], but to our knowledge, have not been applied specifically to O_3 production in an O&NG basin. The principle advantage to OPE is that it is an observable quantity that should differentiate between air parcels of different VOC composition and NO_x mixing ratios, for example, those influenced by O&NG versus urban emissions. However, OPE derived from field observations is an upper limit as it suffers from artifacts such as depositional NO_y loss.

Box model analyses are a common tool used to assess the sensitivity of O_3 production to NO_x and VOC emissions within air parcels of known composition. They have been used recently to model O_3 production in western U.S. O&NG basins during winter months [*Carter and Seinfeld*, 2012; *Edwards et al.*, 2013, 2014]. To our knowledge, a box model analysis has not been previously reported for summertime O_3 production in an O&NG basin. Box models have the advantage of a fully explicit chemical mechanism, but they parameterize transport as a highly simplified, single dilution term. They therefore do not represent heterogeneity in the spatial distribution of emissions. They also do not rely on emission inventories, which can be an important source of uncertainty in three-dimensional chemical transport models [e.g., *Ahmadov et al.*, 2015], but parameterize emissions so as to match observations or constrain primary species to observed values. Box model analyses are useful in assessing the NO_x and VOC sensitivities of O_3 and other secondary products (e.g., acetone, MEK, and $RONO_2$) for averaged data, in which chemical and meteorological variabilities average to typical values [*Edwards et al.*, 2013], or in simulations of air parcel evolution along a known trajectory [*Washenfelder et al.*, 2011b]. In these cases, box models provide a simple alternative to 3-D chemical transport models.

We present a combination of VOC OHR and OPE analyses along with an observationally constrained box model to (1) quantify the impacts of O&NG emissions on summertime maximum O_3 and its production efficiency at a specific location within the NFR and (2) evaluate the O_3 sensitivity to NO_x and VOC emissions. This analysis indicates that the influence of O&NG VOCs on regionally produced O_3 is small relative to their contribution to total VOC mass and OHR, but not negligible on the scale relevant to attainment of regional air quality standards.

2. Experimental and Analysis Methods

2.1. Measurement Site

The Boulder Atmospheric Observatory (BAO; 40.05°N, 105.01°W, 1584 m above sea level) [*Kaimal and Gaynor*, 1983] lies roughly 35 km north of Denver and 25 km east of Boulder in the southwest corner of the

Wattenberg Gas Field (Figure 1). The site has a tall (300 m) tower with south facing stationary platforms (booms) at 10, 100, and 300 m for meteorological measurements of temperature, relative humidity, wind speed, and direction. An external carriage mounted on the southwest side of the tower provides a platform for vertically resolved chemical measurements as described further in section S1 in the supporting information.

2.2. Field Campaigns

Measurements at BAO were made in July–August 2012 and July–August 2014, months when the NFR experiences O_3 levels in exceedance of the EPA 8 h O_3 standard [*Colorado Department of Public Health and Environment (CDPHE)*, 2015]. During these two summers, the NFR was studied by three major field campaigns that contributed data to this analysis. Campaign and measurement descriptions can be found below and as a complete list in Table S1 in the supporting information.

2.2.1. SONNE: 2012

The Summer Ozone Near Natural gas Emissions (SONNE) field campaign was conducted at BAO between 27 July and 12 August 2012. Chemical measurements were acquired via inlets mounted 8 m above ground level (agl) on a walkup tower ~10 m south of the main tower. Continuous in situ measurements of a full suite of C_2-C_{10} hydrocarbons, C_2-C_4 oxygenated VOCs, aromatics, C_2-C_3 alkyl nitrates, and dimethyl sulfide were collected via a custom-built, two-channel gas chromatograph-mass spectrometer (GC-MS) [*Gilman et al.*, 2010]. Samples were acquired (5 min) and analyzed (25 min) on a repeating cycle every 30 min. The accuracy and detection limits are compound-dependent but less than 25% and 10 parts per trillion by volume (pptv), respectively [*Gilman et al.*, 2010]. NO_x and NO_2 were measured with a custom-built, multichannel cavity ring-down (CRD) instrument. NO_2 was measured by direct absorption at 405 nm, while NO_x was simultaneously measured in a second channel after conversion of ambient NO to NO_2 via an addition of excess O_3 [*Fuchs et al.*, 2009]. The accuracy and limit of detection for both species were <5% and <30 pptv, respectively. O_3 was measured via UV absorbance by a commercial instrument (Thermo Environmental Instruments, Inc., Model 49c). Methane (CH_4) was measured via CRD spectroscopy using a wavelength-scanned CRD instrument (Picarro, model 1301 m) [*Peischl et al.*, 2012]. Carbon monoxide (CO) was measured by a vacuum ultraviolet fluorescence instrument [*Gerbig et al.*, 1999]. All chemical measurements were collected at a 1 Hz time resolution and averaged to the GC-MS acquisition period of 5 min every half hour.

2.2.2. FRAPPÉ/DISCOVER-AQ: 2014

In July–August 2014 the NSF Front Range Air Pollution and Photochemistry Éxperiment (FRAPPÉ) and the NASA Deriving Information on Surface Conditions from Column and Vertically Resolved Observations Relevant to Air Quality (DISCOVER-AQ) field campaigns conducted aircraft, mobile, and ground-based measurements at over 15 locations across the Front Range. Measurements at BAO took place between 16 July and 15 August 2014 and included surface and vertically resolved observations. CH_4 and CO were measured from the instrument carriage with a commercial CRD instrument (Picarro, model 2401) [*Chen et al.*, 2010, 2013; *Crosson*, 2008]. Gas-phase ammonia (NH_3) was measured from the carriage via infrared absorption with a quantum-cascade laser instrument (QC-TILDAS) [*McManus et al.*, 2008]. NO_x and NO_2 were measured with the same CRD instrument described in section 2.2.1, which also measured O_3 and NO_y. O_3 was measured by conversion to NO_2 in excess NO and subsequent subtraction of ambient NO_2 from the resulting total O_x [*Washenfelder et al.*, 2011a]. NO_y was thermally converted to NO or NO_2 with a quartz heater (650°C) and quantitatively converted to NO_2 via an addition of O_3 [*Wild et al.*, 2014]. The accuracy and detection limit of NO_x, NO_2, and O_3 in 2014 were <5% and <50 pptv, respectively. The NO_y channel had a limit of detection of <200 pptv and an accuracy of 12% based on recent field comparisons to other NO_y instruments [*Wild et al.*, 2014]. Conversion of NO_y in a 650°C quartz oven may have also suffered interference from the unintended conversion of a small fraction (~6%) of NH_3 in the presence of O_3. Uncertainty associated with this artifact is estimated for the NO_y data based on co-located NH_3 and O_3 measurements, but data are not corrected for this potential interference.

In addition to carriage instruments, O_3 lidar (NOAA TOPAZ) [*Alvarez et al.*, 2011; *Langford et al.*, 2015] measurements were made at a ground site ~0.5 km south of the main tower and $j(NO_2)$ photolysis frequencies (National Center for Atmospheric Research (NCAR) filter radiometer [*Shetter et al.*, 2003]) were measured from a trailer parked at the tower base. Lastly, spectral surface albedo measurements derived from a visible (415–1625 nm) Multi-Filter Rotating Shadowband Radiometer [*Harrison et al.*, 1994; *Michalsky and Hodges*,

2013] were made from a NOAA Surface and Radiation Budget Monitoring mobile laboratory [*Augustine et al.*, 2000] parked at BAO for the duration of the campaign.

2.3. Ozone Production Efficiency

Ozone production efficiencies were only derived from 2014 data due to the lack of NO_y measurements in 2012. Chemical observations were averaged to a 1 min time resolution and filtered to include data after noon (12–6 P.M. mountain daylight time (MDT)) during peak O_3 production and sampling altitudes >25 m agl to reduce the influence of deposition to the surface. The slope of the O_x to NO_z correlation at individual, 15 min intervals was used to isolate and derive the OPE of individual air parcels. In contrast to the O_3/NO_z slope defined in previous studies [e.g., *Hirsch et al.*, 1996; *Olszyna et al.*, 1994; *Trainer et al.*, 1993, 1995], the use of O_x accounts for local O_3 titration through reaction of NO with O_3 near NO_x emission sources. Additionally, NO_z, instead of NO_y, normalizes age across different air parcels [*Trainer et al.*, 1993]. However, by not additionally accounting for NO_y removal processes, such as surface deposition of individual NO_y species (e.g., HNO_3), the OPEs derived here are upper limits. Further OPE details are discussed in sections 3.3 and S2.

2.4. Box Model
2.4.1. Model Description and Constraints

Model simulations were performed with the Dynamically Simple Model of Atmospheric Chemical Complexity (DSMACC) [*Emmerson and Evans*, 2009]. DSMACC is a zero dimension box model that uses the Master Chemical Mechanism (MCM v3.3.1) for its chemistry scheme and the NCAR Tropospheric Ultraviolet and Visible Radiation Model (TUV v5.2) [*Madronich et al.*, 1998] for photolysis rates. The MCM is a near-explicit chemical mechanism representing the gas-phase tropospheric degradation of VOCs [*Jenkin et al.*, 2015]. The subset of chemistry used here includes a complete inorganic mechanism and degradation scheme for 50 primary VOCs, with a total of 4002 species and 15,555 reactions.

All DSMACC simulations are initialized at 8 A.M. MDT and integrated forward for 24 h with a 10 min time step. To represent the NFR as a photochemical box, simulations are initialized with and constrained every 30 min to SONNE diel average observations of temperature and mixing ratios of CO, CH_4, 42 non-methane VOCs, and water vapor (derived from 10 m relative humidity measurements). Simulations are constrained to 2012 data only due to lack of speciated VOC measurements in 2014. For comparison, both temperature and observed O_3 mixing ratios were higher in 2012 than 2014 with differences in maximum diel averages (27 July to 12 August 2012 and 2014) of 1°C and 1.8 ppbv, respectively. DSMACC simulations were additionally constrained to SONNE diel average observations of total NO_x, which was partitioned by the model into its components (NO and NO_2) every 10 min assuming photo-stationary state, using $j(NO_2)$, temperature, and O_3. Section S3 provides further information on DSMACC constraints, which force the model to accurately represent primary species whose average concentrations are governed by processes not represented in the box model, such as emissions and horizontal transport.

An additional dilution rate constant was applied to all 4002 model compounds to simulate average vertical transport and loss from the box (as described in section S3.3). A dilution rate constant of $1.05 \times 10^{-4}\,s^{-1}$ was derived from a fit of the model output to the diel average observations of 10 secondary products. These 10 secondary species consist of O_3, six oxygenated VOCs, and three alkyl nitrates, which were initialized to their average observed values (8 A.M. MDT) but not otherwise constrained (see Figure S6). Background mixing ratios of these 10 compounds (Table S3) were also added to the model at the same rate of dilution to account for entrainment and mixing with the residual layer during boundary layer growth. At the fit dilution rate, the average model-to-observation difference for all 10 compounds was -13.7% (for individual compounds, see Table S3). Table S2 summarizes the model treatment of all chemical observations, and Figure 2 illustrates the observed non-methane VOCs in terms of their diel average OHR.

2.4.2. Model Scenarios

Base (Case 1) simulations represent the average chemical composition at BAO and were constrained to diel average chemical and physical observations as described above. In comparison with Case 1 simulations, Cases 2 and 3 (described below) are used to quantify the impact of primary O&NG VOCs on maximum photochemical O_3 production.
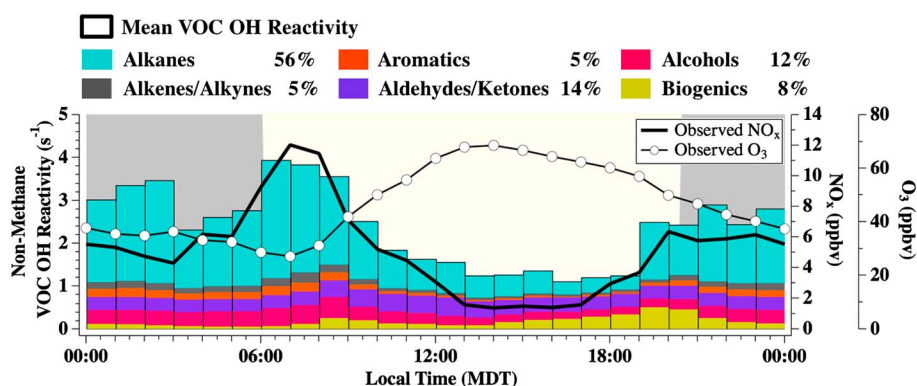
Figure 2. Diel average of non-methane VOC and NO_x model constraints. VOCs (left axis) are given in VOC OH reactivity; NO_x and O_3 (right axes) are given in mixing ratio. The bar height is the average VOC OHR colored by the fractional VOC class contribution every 60 min. Average VOC class contributions are calculated from the sum of averaged (24 h) individual VOCs. VOC OHR does not include contributions from HCHO, CO, or CH_4. Aldehydes and ketones shown here were not used as model constraints but instead used to derive the dilution rate constant.

Case 2 simulations represent the average chemical composition at BAO without primary O&NG VOCs. To derive this VOC scenario, speciated fractions of primary VOCs emitted from O&NG activity were subtracted from Case 1 diel average observations. For example, propane was reduced by 90% between Cases 1 and 2, as 90% of observed propane at BAO was attributed to O&NG emissions [*Gilman et al.*, 2013]. Table S2 provides a full list of speciated O&NG contribution factors. For all non-methane VOCs, *Gilman et al.* [2013] used a multivariate regression with O&NG (propane) and urban (acetylene) tracers to derive O&NG factors. Oxygenated VOCs were not tightly correlated with either tracer and were not assigned an O&NG factor by *Gilman et al.* [2013]. Here the O&NG factors for these compounds have been set to 0%, resulting in a conservative (lower limit) estimate for the attributed O&NG fraction of observed VOCs. In addition, three cycloalkanes, two alkenes, one aldehyde, three biogenic VOCs, and three alkyl nitrates measured during SONNE were not reported by *Gilman et al.* [2013] and are also assigned an O&NG contribution of 0%. The cycloalkanes likely have an O&NG source but minimally impact simulated O_3 due to their small mixing ratios (<0.03 ppbv) and nonexplicit representation in the MCM (section S3.1). For all additional species measured but not explicitly represented in the MCM (see section S3.1), factors were applied to each individual compound prior to lumping. As illustrated in Figure 3, primary O&NG emissions contributed to the majority of alkane OHR (87%) and carbon mixing ratio (86%), but $<25\%$ to all other VOC classes. For CH_4, *Pétron et al.* [2014] quantified the O&NG contribution in the Wattenberg Gas Field as 75% using a combination of aircraft CH_4 observations and a regional bottom-up emission inventory (derived from literature emission factors, Colorado State inventory data, and EPA reported facility-level emission estimates). Here 75% is applied to the observed average diel profile of enhanced CH_4 (minus campaign background of 1814 ppbv). For NO_x, no contribution from O&NG activity was assumed. County level NO_x emissions based on the 2011 (v1) U.S. National Emissions Inventory (further details in section S4) suggest an O&NG contribution of 5.5% to NO_x emissions in the NFR nonattainment area (Figure 1). Past work in a Utah O&NG basin has shown that NO_x emissions from O&NG production can be overestimated by a factor of 4 [*Ahmadov et al.*, 2015], indicating that the 5.5% contribution of O&NG activity to NFR NO_x emissions may be an upper limit.

Case 3 simulations represent the average BAO chemical composition with a doubled contribution from primary O&NG VOCs. For Case 3, speciated factors for primary O&NG VOCs (as described above) were added to Case 1 diel observations. Table S4 provides a numeric comparison of all three VOC scenarios in terms of their non-methane VOC OHR and carbon mixing ratio (ppbC).

3. Results and Discussion

3.1. Observed Chemical Composition and Wind Patterns

Air composition at BAO contains chemical tracers from all regional emission sectors (e.g., O&NG, urban, and agriculture), irrespective of wind direction. The histogram in Figure 4b plots simple chemical tracers for all
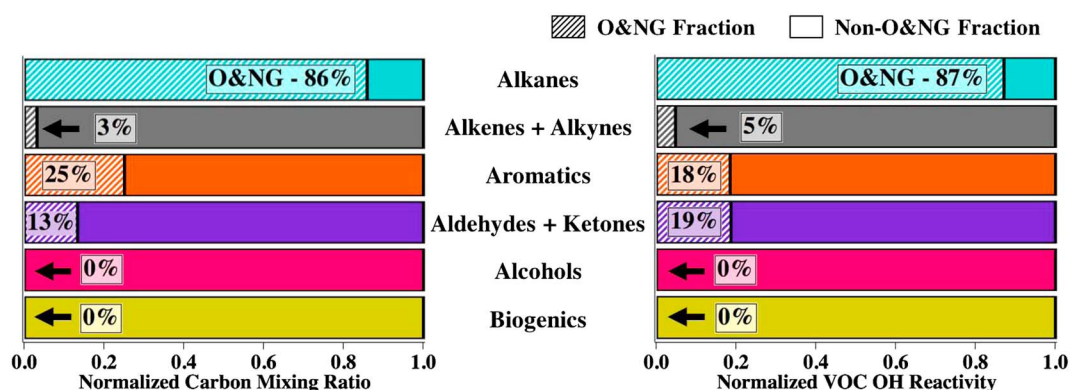
Figure 3. O&NG fraction of observed non-methane VOCs as a function of normalized carbon mixing ratio and VOC OH reactivity. Note that aldehydes and ketones were initialized with Case 1 mixing ratios (assuming O&NG VOC fraction = 0) and calculated by DSMACC in all simulations. The aldehyde and ketone O&NG fractions (OHR: 19% and ppbC: 13%) were derived from a comparison of the Case 1 VOC scenario with the removed O&NG scenario (Case 2) at 2012 observed NO_x mixing ratios.

major emission sectors (O&NG, CH_4; agriculture, NH_3; and urban, CO and NO_x), averaged between 2012 and 2014 observation years, binned by wind direction, and normalized to westerly mixing ratios. Data have been binned by four wind directions and filtered to include wind speeds >2.5 m/s to minimize the influence of nearby emission sources and to be consistent with the threshold used by *Pétron et al.* [2012]. Figure 4b shows that air at the site has a substantial contribution from all regional emission sources irrespective of local north, east, or southerly wind directions. In addition, enhancements of tracers in the direction of each major emission source (e.g., NO_x is slightly enhanced in southerly winds) are smaller than those observed in wintertime [*Brown et al.*, 2013, Figure 7]. These observations suggest significant mixing and recirculation that causes regional air to have characteristics of all surrounding emission sectors.

Several mechanisms serve to mix emissions from different sources within the NFR. During summer, winds follow a typical mountain-valley diel pattern. During the day, thermally driven upslope winds predominately flow from the east, with a slight southerly component [*Toth and Johnson*, 1985]. Beginning in late afternoon, flow patterns turn around and a westerly downslope occurs along the South Platte River Basin, often accompanied by afternoon regional thunderstorm activity [*Toth and Johnson*, 1985]. Figure 4a provides a histogram of 30 min averaged winds measured at BAO during July and August 2012 and 2014 (100 m winds, speed >2.5 m/s, 11 A.M. to 3 P.M. MDT), which illustrate this dominant afternoon easterly flow prior to the downslope switch. A terrain-forced mesoscale vortex circulation pattern, termed the Denver Cyclone, is also a common occurrence during summer months [*Crook et al.*, 1990; *Szoke*, 1991; *Szoke et al.*, 1984; *Wilczak and Glendening*, 1988]. These complex circulation patterns combine to mix air parcels, making it difficult to model the daily evolution of emissions from spatially distinct regional emission source sectors.
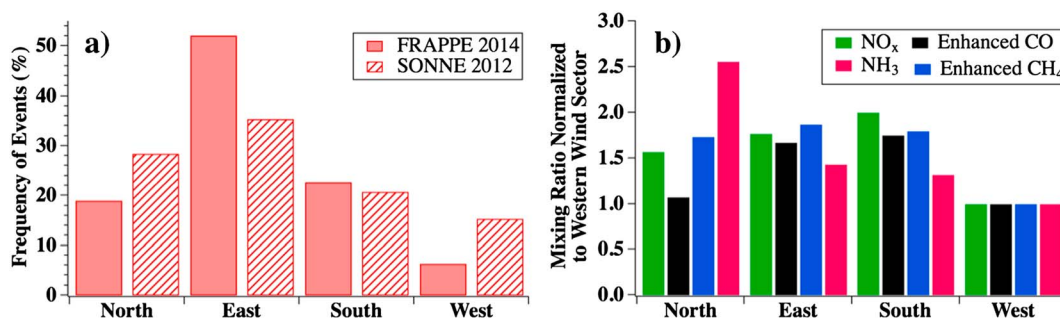

Figure 4. (a) Histogram of July–August 2012 and 2014 wind direction measured at BAO (100 m). (b) Median mixing ratios of chemical tracers averaged between 2012 and 2014 campaign years, normalized to mixing ratios in the western wind sector to illustrate relative sector-to-sector differences on the same scale for all species. CO and CH_4 plotted as normalized enhancements above observed 2012 and 2014 backgrounds. All data filtered for wind speeds of >2.5 m/s. Binned wind directions correspond to north: 315°–45°, east: 45°–135°, south: 135°–225°, and west: 225°–315°.
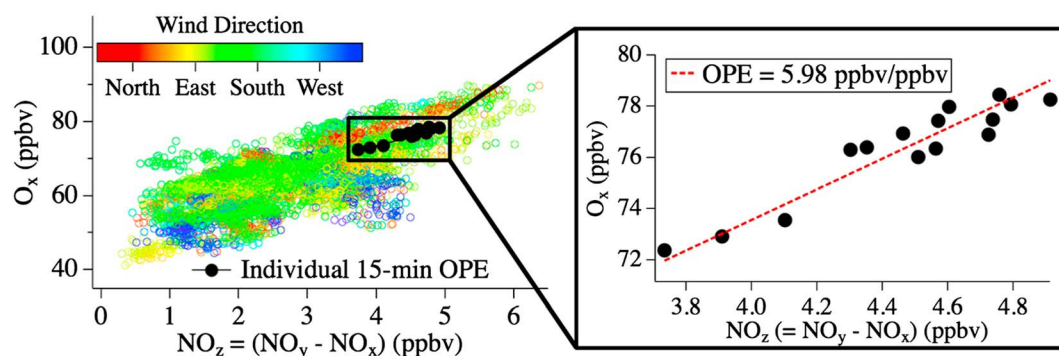
Figure 5. (left) Observed O_x/NO_z correlation for 16 July to 15 August 2014 (12 P.M. to 6 P.M. MDT, $N = 8268$), colored by observed wind direction. (right) Example O_x/NO_z correlation during one, 15 min time interval. This OPE meets the point number (>11), intercept (56.7 ± 9.3 ppbv), and r^2 (>0.5) filter requirements discussed in text.

3.2. VOC OH Reactivity: 2012

The campaign average ($\pm 1\sigma$ standard deviation) OHR for non-methane VOCs (excluding HCHO) observed during SONNE was $2.4 \pm 0.9\,s^{-1}$. This compares to a previous determination at BAO of $3 \pm 3\,s^{-1}$ based on an analysis of data from same instrument in winter 2011 [*Gilman et al.*, 2013] and summertime measurements near O&NG operations in Pennsylvania of $2.4 \pm 1.4\,s^{-1}$ (includes CH_4, excludes HCHO) [*Swarthout et al.*, 2015]. On average, alkanes were the dominant contributing class to VOC OHR (56%; Figure 2), of which the majority can be attributed to primary O&NG emissions (87%: VOC OHR, 86%: ppbC; Figure 3). Biogenic VOCs have been shown to dominate VOC OHR in O&NG regions in Pennsylvania ($47 \pm 22\%$ [*Swarthout et al.*, 2015]) and Texas (70% [*Rutter et al.*, 2015]), but only contribute on average, 8% to VOC OHR at BAO. This result highlights the importance of O&NG emissions relative to biogenic emissions on O_3 production in the NFR, making this location unique compared to two east/southeastern U.S. O&NG basins.

3.3. Ozone Production Efficiency: 2014

During the 2014 campaign, afternoon O_x was correlated with NO_z (Figure 5), typical of summertime relationships between O_3 and oxidized reactive nitrogen observed in other U.S. regions [e.g., *Trainer et al.*, 1993]. Individual OPEs were derived from a two-sided regression fit of O_x to NO_z every 15 min between 12 and 6 P.M. MDT after removing time intervals with fewer than 11, 1 min data points. This time period was chosen to minimize the effects of nonphotochemical factors such as morning O_3 entrainment (see section S2.3.2) and to compare the products of photochemistry (i.e., NO_z and O_3) in distinct air parcels. Increasing the time period to 9 A.M. to 6 P.M. MDT introduces additional scatter in the data from the OPE analyses but does not change the main conclusions presented below. Further, fits with intercepts more than $\pm 2\sigma$ from the mean intercept were also removed, as described further below and in section S2.2. There were 305 OPE fits that met these criteria, which represent at least 15 min of 27 (87%) afternoons in 2014 (see Figure S1). The average ($\pm 1\sigma$) of these 305 OPEs was 2.9 ± 4.4 ppbv/ppbv.

To ensure at least a 98.4% (i.e., significant) probability of correlation, a subset of these OPEs with correlation coefficients (r^2) > 0.5 was also selected. There were 80 OPEs that met the r^2 threshold, which represent at least 15 min of 22 (71%) afternoons in 2014 (see Figure S1). The average ($\pm 1\sigma$) of this 80 OPE subset was 5.3 ± 3.6 ppbv/ppbv. Selection of this subset reduced scatter in the data but also introduced a high bias by eliminating data scattered close to zero (e.g., with small changes in O_x and/or NO_z). We take this smaller 80 OPE subset to represent time periods with the greatest photochemical O_3 production but compare both 305 and 80 OPE populations below. Both populations are representative of the majority of high (>70 ppbv) O_3 days observed at BAO in 2014.

Average OPEs ($\pm 1\sigma$) derived here are similar to those from analyses in other regions of the U.S. However, many previous studies have defined OPE as the slope of O_3/NO_z or O_3/NO_y, making it difficult to directly compare values here to much of the past ~20 years of OPE literature. Nevertheless, the averages of 2.9 ppbv/ppbv (305 OPEs) and 5.3 ppbv/ppbv (80 OPEs) fall within the range of 2–8 ppbv/ppbv for O_x/NO_z previously reported for urban regions across the U.S. [*Kleinman et al.*, 2002; *Nunnermacker et al.*, 1998; *St. John et al.*, 1998; *Zaveri et al.*, 2003].
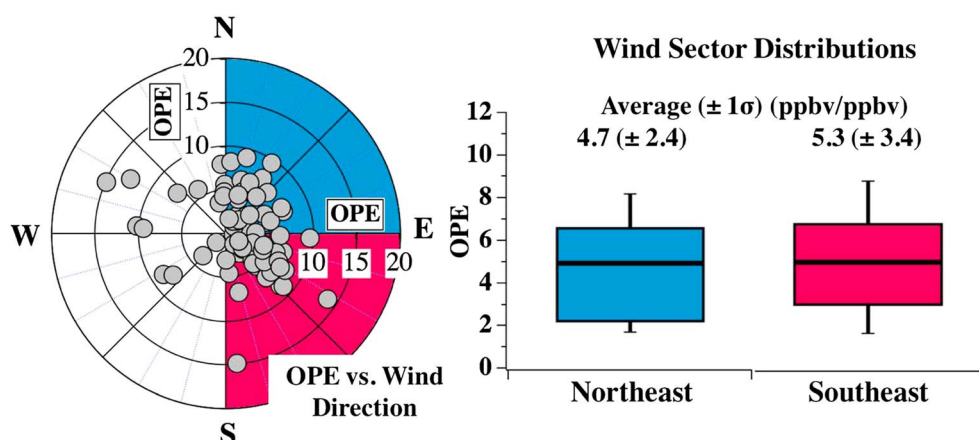
Figure 6. 80 individual OPEs with high ($r^2 > 0.5$) O_x/NO_z correlation plotted radially as a function of wind direction, colored by NE (0–90°, blue) and SE (90–180°, red) wind sectors. The box and whisker plots show the median OPE for each wind sector (SE: 5.1 ppbv/ppbv, NE: 4.9 ppbv/ppbv) and range between the 10th and 90th percentiles.

3.3.1. NFR Emission Sector OPEs

To distinguish the influence of different emission sectors on OPE, individual OPEs were sorted according to two markers of air transport history: (1) wind direction and (2) simple chemical tracers. Sorting the data according to these markers contrasts the O_3 production associated with the relatively different VOC composition and NO_x mixing ratios of O&NG and urban emission sectors. As this section describes, however, any dependence of OPE on these parameters is considerably smaller than the variability and/or uncertainty in the observed OPE data.

3.3.1.1. OPE as a Function of Wind Direction

Air arriving at BAO from the northeast is expected to have traveled over regional O&NG operations, while that from the southeast to have been relatively more urban influenced (Figure 1). However, the OPE measured at BAO does not vary strongly with wind direction. The overall O_x/NO_z correlation in 2014, colored by wind direction (Figure 5, left), does not show a clear difference in air arriving from south or north of the site. Analysis of individual OPEs against wind direction reveals similar results. Figure 6 provides a wind rose of the 80 OPE subset ($r^2 > 0.5$) colored by northeast (NE: 0–90°), southeast (SE: 90–180°), and western (W: 180–360°) wind directions (15 min average). The box and whisker plots for NE and SE wind sectors show no statistically significant (i.e., $p > \alpha$, $\alpha = 0.05$) difference in their average (difference = 0.6 ppbv/ppbv, $p = 0.43$) or median (difference = 0.1 ppbv/ppbv, $p = 0.88$) values. In addition, there is no significant difference between average NE and SE OPEs (difference = 0.5 ppbv/ppbv, $p = 0.39$) when calculated from the larger population of 305 without the r^2 selection. Due to the large observed variability in OPE, 95% confidence intervals for differences in mean NE and SE OPEs are 0.6 ± 1.4 ppbv/ppbv and 0.5 ± 1.1 ppbv/ppbv for the 80 and 305 OPE populations, respectively. This wind direction analysis suggests a 95% probability that the OPE influence of O&NG emissions is less than 1.8 ppbv/ppbv. During times of high photochemical activity in 2014 (e.g., highest NO_z mixing ratios; Figure 5), an OPE less than 1.8 ppbv/ppbv suggests that the O&NG sector contributes at most 11 ppbv to total O_3. The actual O&NG influence determined from the box model analysis is likely considerably smaller (see section 3.4.2).

Due to the complexity of local air trajectories, including diel flow patterns that mix urban and O&NG emissions (section 3.1), it is difficult to accurately determine air transport and mixing histories using observed wind directions alone. A back trajectory model has the potential to track air transport history more accurately than local wind direction. As with observed wind direction, wind sectors for the 80 OPE subset as defined by a back trajectory model (described in section S5) show no statistically significant difference between average OPEs from the NE and SE wind sectors (difference = 0.6 ppbv/ppbv, $p = 0.55$; Figure S9).

The lack of statistically significant difference in observed OPE with observed or modeled wind direction is evidence for mixing between air parcels that obscures quantifiable differences between urban and O&NG sectors and/or an OPE effect from O&NG emissions that has a 95% probability of being less than 1.8 ppbv/ppbv. We interpret these results to mean either (1) observed OPEs are the product of both urban and O&NG emissions that were well-mixed prior to measurement at BAO or (2) an OPE influence of urban and O&NG emissions that are similar enough (i.e., <1.8 ppbv/ppbv) to be obscured by mixing when air is transported to BAO.
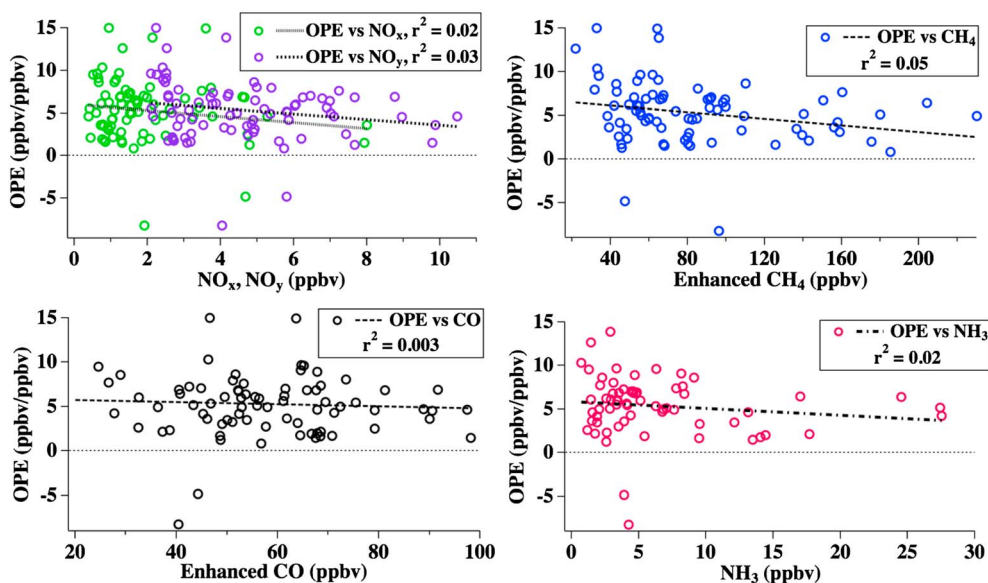
Figure 7. 80 individual OPEs with high ($r^2 > 0.5$) O_x/NO_z correlation as a function of simple chemical tracers. CH_4 and CO mixing ratios are the enhancements above background. Correlation coefficients (r^2) for all species suggest no statistically significant trend (95% confidence level) in OPE with tracers.

The box modeling results discussed in section 3.4.3 are consistent with the second scenario and suggest an O&NG influence on regional average OPE of 1.3 ppbv/ppbv.

3.3.1.2. OPE as a Function of Chemical Tracers

Chemical tracers provide an additional method to determine air transport history. In the NFR, CH_4 is emitted primarily by O&NG (see above section 2.4.2), NH_3 by agriculture, and CO and NO_x by urban activity. Background mixing ratios (minimum observed campaign values) of CO (76 ppbv) and CH_4 (1916 ppbv) were subtracted prior to analysis. Figure 7 shows correlations of the 80 OPE subset with NO_x, NO_y, NH_3, CH_4, and CO. Correlations visually indicate a slight decrease in OPE with increasing tracer mixing ratios; however, correlation coefficients indicate no statistically significant trend at the 95% confidence level ($p > 0.05$). Correlations between chemical tracers and the 305 OPE-population are also insignificant ($p > 0.22$). These results indicate relatively well-mixed air, also suggested by the dominant easterly flow and nondirectionally enhanced tracer mixing ratios shown in Figure 4.

A second possibility is that these tracers are not specific enough to their assigned emission sectors. As previously discussed in *Pétron et al.* [2012, 2014], approximately 25% of CH_4 emissions are not associated with O&NG operations, including three landfills located approximately 3 km to the south-southwest of BAO. In addition, NEI-2011 inventories attribute 27% of NO_x emissions in Weld County (Figure 1) to O&NG operations (section S4). Ideally, this analysis would be conducted with more specific chemical tracers not available in 2014 (e.g., O&NG: propane and urban: acetylene) but suggests that simple tracers used here do not uniquely distinguish the influence of different emission sectors on observed OPE at BAO.

3.3.2. Uncertainty in OPE Analysis

Interpretation of the O_x/NO_z relationship is subject to several limitations [*Ryerson et al.*, 1998; *Trainer et al.*, 1993] that are presented below in terms of their relation to deriving an average OPE under NFR conditions.

First, variability in background O_3 may complicate OPE analysis [e.g., *Neuman et al.*, 2009]. Backgrounds are represented by the intercept of the O_x/NO_z correlation and will artificially change the OPE if one fit is applied to air parcels with different backgrounds (see example Figure S2). Therefore, OPE was derived from short time intervals (15 min) and filtered for intercepts greater than 2σ from the mean O_x background (further details in section S2.2) in order to isolate air parcels with similar O_3 backgrounds.

Second, O_x is not always positively correlated with NO_z. This is likely the result of (1) environmental conditions that do not promote photochemical activity and/or (2) transport processes that mix air parcels with differences in background O_3 mixing ratios similar to their photochemical O_3 enhancements.
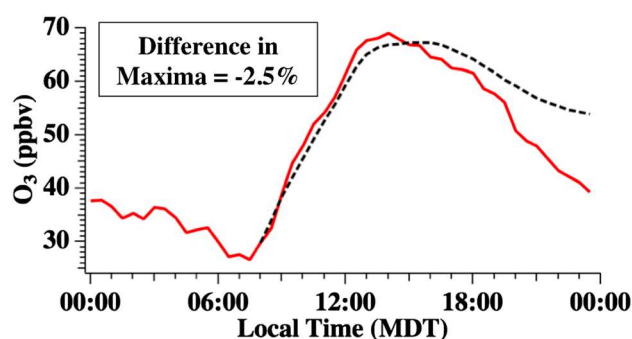
Figure 8. Base case (Case 1) simulated O_3. Observed diel average (red) and Case 1 simulated (black dashed) mixing ratios. Difference between observed and modeled maxima is −2.5%.

Summer 2014 in the NFR was unseasonably cool with high thunderstorm activity (Figure S5), which can enhance the downwind transport of O_3 but also inhibit the stagnation and accumulation of pollution that contributes to OH radical generation and efficient O_3 production. These environmental conditions can lead to periods of time with moderate photochemical activity and O_3 production of only a few ppbv, similar to the variability observed in 2014 background O_3 (O_x background: 56.7 ± 9.3 ppbv (2σ)). Mixing and/or sampling of these air parcels remove any observable O_x/NO_z correlation. The r^2 filter is applied to remove these events but by doing so, biases the 80-OPE average high.

Third, OPE is sensitive to HNO_3 deposition [e.g., *Neuman et al.*, 2009; *Sillman et al.*, 1998; *Trainer et al.*, 1993]. Preferential removal of HNO_3 relative to O_3 will artificially raise the O_x/NO_z slope since HNO_3 is frequently the largest NO_z component in summer. A deposition velocity of 1–5 cm s^{-1} within a 2 km boundary layer provides an upper limit estimate of 11–52% of NO_z lost over 6 h of transport (further details, see section S2.3.1). Recalculating individual OPEs with corrected NO_z produces an average ($\pm 1\sigma$) OPE range of 3.3 ppbv/ppbv (± 2.2) to 4.7 ppbv/ppbv (± 3.2) for the highly correlated 80-OPE subset, lower than the original average of 5.3 ppbv/ppbv but within the standard deviation of 3.6 ppbv/ppbv. Additional, unintended conversion of NH_3 may also occur in the presence of ambient O_3 at temperatures of 650°C in the CRD NO_y quartz oven. Adjusting NO_z measurements of the original 80 OPEs with concurrent NH_3 and O_3 measurements (further details in section S2.3.1) increases the average to 5.9 ppbv/ppbv. Combination of HNO_3 and NH_3 artifacts suggests that the average OPE for the highly correlated subset is between 3.3 and 5.9 ppbv/ppbv (−2.0/+0.6), a range encompassed by the standard deviation ($1\sigma = 3.6$ ppbv/ppbv) of the originally derived average.

An analysis of the 2014 data provides an average and expected distribution of observed OPE at BAO but does not distinguish the influence of urban emissions from the O&NG sector. This result does not change with the selection of highly correlated OPEs. These observations lead to three possible conclusions: (1) based on observational and modeled-wind direction analyses, the OPE difference between O&NG and urban emission sectors has a 95% probability of being within 1.8 ppbv/ppbv; (2) OPE differences are obscured by regional air mixing; and/or (3) small OPE differences cannot be distinguished using simple chemical tracers with multiple emission sources. Although OPE does not statistically vary with either wind direction or chemical tracer analyses, the similarity provides a point of comparison between the observations and box model simulations described below.

3.4. Box Model Simulations: Maximum Photochemical O_3

Model simulations were constrained to SONNE diel average observations as described in section 2.4.1. With the dilution rate constant derived from a fit to 10 secondary species, the Case 1 VOC scenario simulates maximum O_3 to within −2.5% (−1.7 ppbv) of the SONNE diel average. The average relative deviation between the model output and observations for O_3 is −2.6% (11 A.M. to 3 P.M. MDT, ±2 h from solar noon). Figure 8 illustrates the observed diel average and model output for O_3, which suggests an accurate base case simulation of maximum O_3 produced at BAO. Deviation between simulated and observed O_3 profiles after 4 P.M. MDT is the result of the constant dilution/background-O_3 entrainment rate that is applied to the entire 24 h simulation, as described in section S3.3.

3.4.1. NO_x Sensitivity

Case 1 simulations were run while constrained to SONNE observed mixing ratios of VOCs, NO_x, and temperature (as described in section 2.4). To test the sensitivity of maximum photochemical O_3 to NO_x, 11 simulations were run with the Case 1 VOC scenario, scaling observed NO_x mixing ratios (displayed in Figure 2) by a factor of 0 to 5. As shown in Figure 9 and Table S6, observed SONNE NO_x mixing ratios (NO_x scaling factor $= 1$) produce a maximum of 16.7 ppbv of photochemical O_3, while doubling observed NO_x increases photochemical
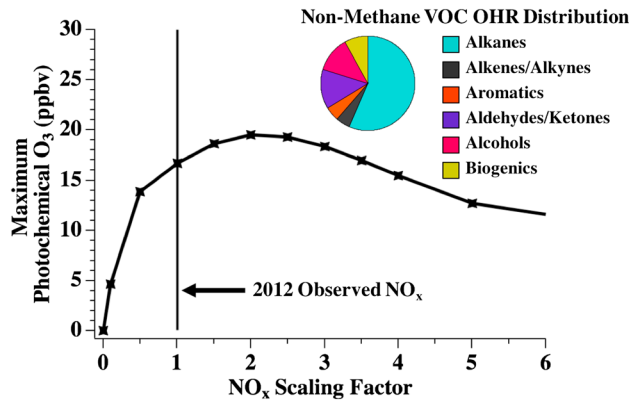
Figure 9. NO_x sensitivity of maximum photochemical O_3 in the base case (Case 1) simulation. Eleven simulations are shown with SONNE (2012) observed NO_x mixing ratios, represented by a scaling factor of 1, scaled from 0 to 5. The pie chart insert represents the 24 h average fractional contribution of non-methane VOCs to OH reactivity.

O_3 to 19.5 ppbv. Here photochemical O_3 is defined as the difference between simulated O_3 and the simultaneous mixing ratio of O_3 in the zero-NO_x simulation. Photochemical O_3 production does not occur without NO_x; however, O_3 is introduced to the model to simulate entrainment of background O_3 into the boundary layer (see section S3.3). O_3 entrainment occurs at the same rate in each simulation and is therefore represented by the zero-NO_x simulation. Subtracting these mixing ratios from each nonzero-NO_x simulation provides the photochemically produced O_3 for the given amount of NO_x.

Figure 9 suggests that photochemical O_3 production in the region surrounding BAO is NO_x limited. An increase or decrease in NO_x by a factor of 2 leads to a 16.8% (±2.8 ppbv) change in maximum photochemical O_3. However, NO_x increases above a factor of 2 move O_3 production into the NO_x saturated (VOC sensitive) photochemical regime, such that further increases will reduce maximum O_3. These results are consistent with NO_x sensitivities derived from previous 3-D modeling of NFR O_3 with a 2010 emission scenario [*Colorado Department of Public Health and Environment (CDPHE)*, 2008].

3.4.2. O&NG Influence

To determine the average influence of O&NG emissions on maximum photochemical O_3, the fraction of VOCs attributed to primary O&NG emissions was removed (Case 2) and doubled (Case 3) as described in section 2.4.2. Twenty-two additional simulations were run with these two VOC scenarios while scaling SONNE observed NO_x mixing ratios between 0 and 5. Results of these simulations in comparison to Case 1 from Figure 9 are listed in Table S6 and shown in Figure 10. The pie chart inserts represent the 24 h average, non-methane VOC-class fractional contribution to VOC OHR and carbon mixing ratio (ppbC) for each VOC scenario. At observed NO_x mixing ratios, the difference in maximum photochemical O_3 between Cases 1 and 2 (no O&NG VOC emission contribution) is 17.4%, or a 2.9 ppbv decrease. Similar to maximum O_3, the O&NG VOC influence
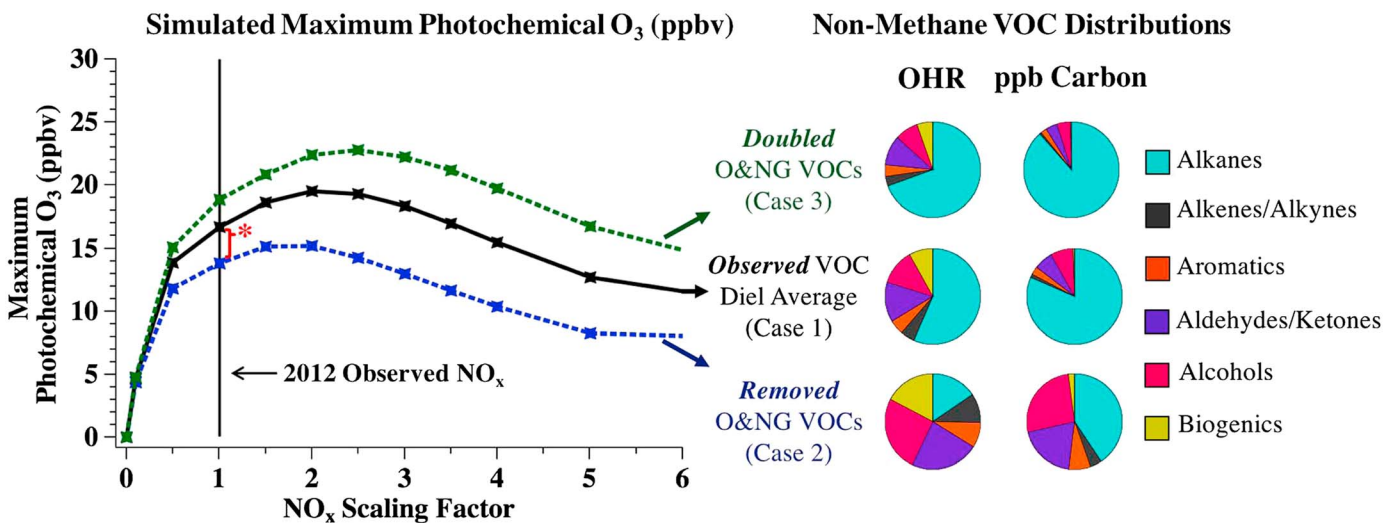

Figure 10. NO_x sensitivity of simulated maximum photochemical O_3 mixing ratios for three VOC scenarios. The asterisk indicates a difference of 17.4% between observed VOC base case (Case 1) and VOC scenario with O&NG VOCs removed (Case 2) at SONNE (2012) observed NO_x mixing ratios. The pie chart inserts illustrate the 24 h average non-methane VOC OHR (s^{-1}) and carbon mixing ratio (ppbC) of each VOC scenario. Distributions do not include CH_4, CO, or HCHO.
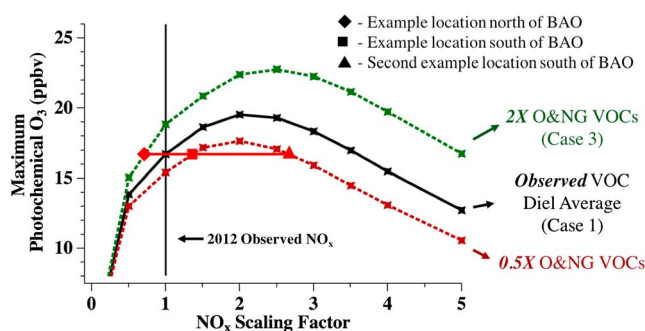
Figure 11. NO_x sensitivity curves for three VOC scenarios. In contrast to Figure 10, the third VOC scenario has O&NG VOCs reduced by half instead of completely removed. The red line and symbols provide example locations to the north and south of BAO with different O&NG and NO_x mixing ratios that experience the same photochemical O_3 enhancement as that at BAO.

on photochemical MDA8 (maximum daily 8 h average) is a decrease of 18.4% or 2.5 ppbv. Doubling the mixing ratio of O&NG VOCs increases simulated maximum photochemical O_3 by 13.2% or 2.2 ppbv, indicating a nonlinear change in O_3 with O&NG VOCs. These three VOC scenarios suggest that while O_3 production is sensitive to NO_x, maximum and MDA8 O_3 mixing ratios will also respond to reductions in O&NG VOCs, again consistent with previous 3-D model results [*Colorado Department of Public Health and Environment (CDPHE)*, 2008].

The 16.7 ppbv of photochemical O_3 produced in Case 1 represents the maximum O_3 enhancement under average conditions. However, 2014 observed O_3 mixing ratios (Figures 5 and S1) show that O_3 enhancements above background can be approximately 30 ppbv on days with high photochemical activity (e.g., high O_3 and NO_z mixing ratios). As described below in section 3.4.4 and section S7, model sensitivity studies show that photochemical O_3 is highly sensitive to photolysis rates, potentially explaining the large enhancements on days with photolysis rates larger than average values. In contrast, the O&NG VOC contribution to O_3 (~20%) is not highly sensitive to photolysis rates (section 3.4.4). Therefore, assuming mixing ratios of VOCs and NO_x similar to their observed diel average values, the absolute contribution from O&NG VOCs could be ~6 ppbv on photochemically active days with ~30 ppbv of regional photochemical O_3 production.

The total contribution of O&NG activity to photochemical O_3 will depend on emissions of NO_x as well as VOCs. The difference of 17.4% highlighted in Figure 10 assumes no change in NO_x from observed mixing ratios. Applying NO_x reductions of 5.5% based on EPA NEI-2011 inventories (see section 2.4.2), Cases 1 and 2 suggest that O&NG activity contributes 18.6% (3.1 ppbv) to maximum photochemical O_3, in comparison to 17.4% (2.9 ppbv) from VOC emissions alone. However, NEI inventory estimates of O&NG NO_x emissions may be overestimated [e.g., *Ahmadov et al.*, 2015]. Thus, the total O&NG contribution to modeled maximum photochemical O_3 at diel average mixing ratios of NO_x and VOCs is between 17.4 and 18.6% or 2.9 and 3.1 ppbv.

As shown in Figure 10, alkanes contributed 82% to the average SONNE non-methane carbon mixing ratio measured at BAO (Figure 10, pie chart), of which 86% are attributed to O&NG emissions (Figure 3). Despite this dominant fraction, the alkane contribution to average non-methane VOC OHR was 56% and less than 18% to maximum photochemical O_3. This result is consistent with previous literature showing that alkanes are not efficient at producing O_3 [e.g., *Russell et al.*, 1995] and demonstrates the difficulty in using either carbon mixing ratio or VOC OHR for attribution of photochemically produced O_3 to O&NG VOC emissions.

Despite evidence for reasonably well-mixed urban and O&NG emissions, Figure 1 suggests spatial heterogeneity in emissions from these sources, which can result in different photochemical regimes for O_3 production. For example, NO_x and urban VOCs are expected in larger concentrations ~30 km south of BAO near urban-Denver [*Brown et al.*, 2013; *Swarthout et al.*, 2013], while O&NG VOCs may be larger ~50 km north of BAO centered in the Wattenberg Gas Field near Greeley [*Swarthout et al.*, 2013]. However, O_3 levels in exceedance of NAAQS occur across these same distances [*Colorado Department of Public Health and Environment (CDPHE)*, 2015], suggesting a level of regional similarity in O_3 enhancements. Buffering effects in the VOC-NO_x sensitivity curves (Figure 11) can explain regional O_3 enhancements despite different photochemical regimes. Figure 11 shows that if, for example, the absolute mixing ratios of non-O&NG VOCs remained the same but O&NG VOCs were doubled and NO_x reduced by 30% (Figure 11, red diamond), the model predicts the same maximum O_3 produced as that at BAO. This implies that north of BAO, with a potentially larger abundance of O&NG VOCs, this region would be more sensitive to NO_x emission reductions. In contrast, if the non-O&NG VOCs remained the same but O&NG VOCs were reduced by 50% at two southern locations, the model predicts nearly the same maximum O_3 produced for NO_x emissions 1.3 to 2.7× higher than those at BAO

Table 1. Box Model Sensitivity Study Results[a]

			Δ Max Photochemical O_3		
Parameter	Base Case Value	Value Adjustment	(ppbv)	(%)[b]	Δ OPE (%)[b]
Photolysis rates	8 A.M. MDT values: $j(NO_2) = 3.6 \times 10^{-3} \, s^{-1}$ $j(O^1D) = 4.0 \times 10^{-6} \, s^{-1}$	±25%	+6.0/−5.4	+35.9/−32.3	+4.6/−3.1
		±10%	±2.3	±13.8	±1.5
Dilution	$k = 1.05 \times 10^{-4} \, s^{-1}$	±10%	+1.3/−1.1	+7.8/−7.1	-
Temperature	SONNE observations	±10%	±0.8	±4.8	+7.7/−6.2
Background O_3	58 ppbv	±10%	±0.1	±0.6	±3.1
Enhanced CH_4	SONNE observations-background	±10%	±<0.1	-	-
		±75%	±0.1	±0.6	-
O_3 deposition	$k = 3.5 \times 10^{-6} \, s^{-1}$	±10%	±<0.1	-	-
Albedo	0.067	±10%	±<0.1	-	-
HNO_3 deposition	$k = 2.2 \times 10^{-5} \, s^{-1}$	−100%	− <0.1	-	+7.7[c]

[a]Calculated for Case 1 VOC scenario at NO_x scaling factor = 1.
[b]Values not provided if change is <0.1 ppbv (max photochemical O_3) or <0.1 ppbv/ppbv (OPE).
[c]HNO_3 deposition artificially increases modeled OPE by 7.7%; all OPE simulations were run without HNO_3 deposition as this does not change photochemical O_3 and is necessary to accurately model OPE.

(Figure 11, red box and triangle). O_3 production at the second of these points (red triangle) is in the NO_x-saturated regime but still produces the same photochemical O_3 as at the NO_x-limited BAO. These scenarios suggest that O_3 enhancements in the NFR can be regional, while effective control strategies should still be informed by finer scale VOC/NO_x observations.

3.4.3. Model Ozone Production Efficiency

Case 1 and 2 simulations, as described above, were used to calculate the influence of O&NG VOC emissions on modeled OPEs. The OPE of each model simulation was calculated from the average $\Delta O_x/\Delta NO_z$ ratio between 11 A.M. to 3 P.M. MDT, the same time period during which the model was fit to best reproduce 10 secondary products (see section S3.3). Here ΔO_x and ΔNO_z are used to capture photochemical O_3 production and NO_x oxidation. Delta O_x and ΔNO_z are defined as the difference between the O_x and NO_z mixing ratios in a given simulation and the simultaneous values in the zero-NO_x simulation (as described in section 3.4.1). The HNO_3 dilution rate constant was the same as all other 4001 species ($k = 1.05 \times 10^{-4} \, s^{-1}$), but its deposition rate was set to $0 \, s^{-1}$ to remove the influence of HNO_3 loss on NO_z. Eliminating HNO_3 deposition does not impact simulated maximum photochemical O_3 but does increase Case 1 OPE by 7.7% (see Table 1). Simulated OPE was also found to decrease with increasing NO_x mixing ratios, consistent with previous OPE model simulation results [e.g., *Lin et al.*, 1988].

At a NO_x scaling factor of 1, OPEs derived from the Case 1 and 2 VOC scenarios are 6.5 ppbv/ppbv (±0.5) and 5.2 ppbv/ppbv (±0.5), respectively. The errors are derived from the quadrature addition of OPE uncertainties associated with model parameters listed in Table 1 (not including HNO_3 deposition). These results suggest that O&NG VOC emissions increase the efficiency of O_3 production at BAO by 1.3 ppbv/ppbv (20%). To account for NEI-estimated O&NG NO_x emissions (see section 2.4.2), the OPE for Case 2 (no O&NG VOCs) was calculated at a NO_x scaling factor of 0.945 (−5.5%). The OPE influence of O&NG emissions did not change, as this small NO_x reduction did not influence the simulated OPE by >0.1 ppbv/ppbv. The similarity between Cases 1 and 2 suggests that the OPE influence of O&NG emissions is small enough to be obscured in observations at BAO due to air transport and mixing, as discussed previously in section 3.3.1.1.

3.4.4. Model Sensitivity Studies

As described above, simulations for all three VOC scenarios were constrained every 30 min to chemical species and physical parameters. The only tunable model parameter was the dilution rate constant, which was derived by minimizing the deviation between observations and model output for 10 select secondary products, including O_3. A ±10% change in the dilution rate constant changes simulated maximum photochemical O_3 in Case 1 by +1.3/−1.1 ppbv (+7.8/−6.6%) and average model-to-observation relative deviation of all 10 compounds by +1.6/−1.2%.

Case 1 (at observed NO_x mixing ratios) was additionally tested for sensitivities to ±10% changes in other model constraints including photolysis rates, albedo, temperature, background O_3, enhanced CH_4, and O_3/HNO_3

deposition rates (see Table 1). Sensitivity differences between maximum photochemical O_3 and OPE can be explained by the additional dependence of OPE on photochemical NO_x oxidation. Of the parameters tested, OPE is most sensitive to changes in temperature, while maximum photochemical O_3 is most sensitive to changes in photolysis rates (more than the dilution rate constant) and increases by as much as 13.8% with a 10% increase in both $j(NO_2)$ and $j(O^1D)$ scaling factors. Observations of $j(NO_2)$ and $j(O^1D)$ are not known with greater than 25% accuracy, which will change absolute maximum photochemical O_3 by $+6.0/-5.4$ ppbv ($+35.9/-32.3\%$). To test the sensitivity of the main box model results to photolysis rates, 15 additional simulations were run for Cases 1 and 2, while scaling photolysis rates by $\pm25\%$. The difference in maximum photochemical O_3 between Cases 1 and 2 is not as sensitive to changes in photolysis as is the absolute maximum simulated O_3 (Figures S10 and S11). In other words, regardless of 25% changes in photolysis rates, BAO photochemical O_3 remains sensitive to NO_x (Figure S10) and the O&NG VOC influence ranges from 15.1 to 19.4% (Figure S11), within 2.3% of 17.4% derived under original photolysis conditions.

4. Conclusions

The Northern Front Range of Colorado has been in nonattainment with the NAAQS for O_3 since 2007. Summertime photochemical O_3 in the NFR is influenced by regional NO_x emissions, concentrated around urban-Denver, and large VOC emissions from a rapidly developing O&NG basin. The BAO site lies between these major regional emission sectors and exhibits influence from each (O&NG, urban, and agriculture). Data from this site were used to quantify the influence of O&NG emissions on O_3 production using an observationally constrained box model and metrics of VOC OHR and OPE.

OPEs derived from 2014 O_x/NO_z correlations at 15 min time intervals during 27 afternoons have an average of 2.9 ± 4.4 ppbv/ppbv (1σ) for all determinations and 5.3 ± 3.6 ppbv/ppbv ($-2.0/+0.6$) for a smaller subset with high correlation between O_x and NO_z. A difference in average OPE could not be statistically distinguished for air primarily influenced by O&NG and urban emissions using observed wind direction, modeled back-trajectories, or simple chemical tracers. These results suggest that the OPE influence of O&NG and urban emissions at BAO is obscured by air mixing and/or do not differ to within 1.8 ppbv/ppbv. The simulated OPE difference of 1.3 ppbv/ppbv with and without O&NG primary VOCs falls within the uncertainty of the 2014 observational analyses.

Box model simulations constrained to diel average chemical and physical observations indicate that maximum photochemical O_3 at BAO is NO_x sensitive. Simulations with removed and doubled primary O&NG VOC contributions showed that O&NG VOC emissions contribute on average 17.4% (2.9 ppbv) to maximum photochemical O_3 and scale nonlinearly with changes in O&NG VOCs. NEI emissions of O&NG NO_x are estimated to contribute up to an additional 1.2% (0.20 ppbv) to the total contribution of O&NG activity to maximum O_3 photochemically produced at BAO. Alkanes contributed on average 82% to the observed carbon mixing ratio, of which 86% could be attributed to O&NG emissions. However, alkanes only contributed 56% to VOC OHR and less than 18% to modeled maximum photochemical O_3.

Future work in the NFR is required to address several key uncertainties. First, detailed multiyear studies are required to assess the influence of rapid changes in O&NG and urban activities on ambient levels of VOCs and NO_x and the sensitivity of photochemical O_3 production. Between 2012 and 2014, the number of active wells in Weld County increased by ~2000, oil production more than doubled, and natural gas production increased by a factor of ~1.6 [*Colorado Oil and Gas Conservation Commission (COGCC)*, 2/2016]. Since early 2015, O&NG drilling activity has declined nationwide. In addition, the NFR population has increased by 12% to over 3 million people since 2010 [*United States Department of Agriculture (USDA)*, 2016] and continues to grow, influencing the absolute emissions of NO_x and distribution across the region. Such rapid changes in O&NG activity and urban development suggest the potential for year-to-year changes in photochemical O_3 sensitivities and emissions of VOC and NO_x.

Second, spatially distributed studies from across the region are required to understand the differences in O_3 sensitivities in the more VOC impacted areas to the north and NO_x impacted areas to the south. Analysis of recent 2014 and 2015 field studies should be informative. Future studies incorporating the type of detailed measurements and models presented here at ground sites that span the NFR would serve to improve the

understanding of regional O_3 production sensitivities to VOCs and NO_x, as well address recent trends in emissions of both urban and O&NG NO_x and VOCs.

List of Primary Acronyms

BAO –Boulder Atmospheric Observatory
CRD –Cavity Ring Down
DISCOVER-AQ –Deriving Information on Surface Conditions from Column and Vertically Resolved Observations Relevant to Air Quality
DSMACC –Dynamically Simple Model of Atmospheric Chemical Complexity
EPA –Environmental Protection Agency
FRAPPÉ –Front Range Air Pollution and Photochemistry Éxperiment
MCM –Master Chemical Mechanism
MDA8 –Maximum Daily 8-h Average
MDT –Mountain Daylight Time
NAAQS –National Ambient Air Quality Standard
NEI –National Emission Inventory
NFR –Northern Front Range
O&NG –Oil and Natural Gas
OHR –VOC OH Reactivity
OPE –Ozone Production Efficiency
ppbC –parts per billion of Carbon
SONNE –Summer Ozone Near Natural gas Emissions
TUV –Tropospheric Ultraviolet and Visible radiation model
VOC –Volatile Organic Compound

References

Ahmadov, R., et al. (2015), Understanding high wintertime ozone pollution events in an oil- and natural gas-producing region of the western US, *Atmos. Chem. Phys.*, 15(1), 411–429, doi:10.5194/acp-15-411-2015.

Alvarez, R. J., et al. (2011), Development and application of a compact, tunable, solid-state airborne ozone lidar system for boundary layer profiling, *J. Atmos. Oceanic Technol.*, 28(10), 1258–1272, doi:10.1175/Jtech-D-10-05044.1.

Augustine, J. A., J. J. DeLuisi, and C. N. Long (2000), SURFRAD—A national Surface Radiation Budget Network for atmospheric research, *Bull. Am. Meteorol. Soc.*, 81(10), 2341–2357, doi:10.1175/1520-0477(2000)081<2341:SANSRB>2.3.CO;2.

Brantley, H. L., E. D. Thoma, and A. P. Eisele (2015), Assessment of volatile organic compound and hazardous air pollutant emissions from oil and natural gas well pads using mobile remote and on-site direct measurements, *J. Air Waste Manage.*, 65(9), 1072–1082, doi:10.1080/10962247.2015.1056888.

Brown, S. S., et al. (2013), Nitrogen, Aerosol Composition, and Halogens on a Tall Tower (NACHTT): Overview of a wintertime air chemistry field study in the front range urban corridor of Colorado, *J. Geophys. Res. Atmos.*, 118, 8067–8085, doi:10.1002/jgrd.50537.

Butler, T. J., F. M. Vermeylen, M. Rury, G. E. Likens, B. Lee, G. E. Bowker, and L. McCluney (2011), Response of ozone and nitrate to stationary source NOx emission reductions in the eastern USA, *Atmos. Environ.*, 45(5), 1084–1094, doi:10.1016/j.atmosenv.2010.11.040.

Carlton, A. G., E. Little, M. Moeller, S. Odoyo, and P. B. Shepson (2014), The data gap: Can a lack of monitors obscure loss of Clean Air Act benefits in fracking areas? *Environ. Sci. Technol.*, 48(2), 893–894, doi:10.1021/es405672t.

Carter, W. P. L., and J. H. Seinfeld (2012), Winter ozone formation and VOC incremental reactivities in the Upper Green River Basin of Wyoming, *Atmos. Environ.*, 50, 255–266, doi:10.1016/j.atmosenv.2011.12.025.

Chameides, W. L. (1978), The photochemical role of tropospheric nitrogen oxides, *Geophys. Res. Lett.*, 5(1), 17–20, doi:10.1029/GL005i001p00017.

Chen, H., et al. (2010), High-accuracy continuous airborne measurements of greenhouse gases (CO2 and CH4) using the cavity ring-down spectroscopy (CRDS) technique, *Atmos. Meas. Tech.*, 3(2), 375–386, doi:10.5194/amt-3-375-2010.

Chen, H., A. Karion, C. W. Rella, J. Winderlich, C. Gerbig, A. Filges, T. Newberger, C. Sweeney, and P. P. Tans (2013), Accurate measurements of carbon monoxide in humid air using the cavity ring-down spectroscopy (CRDS) technique, *Atmos. Meas. Tech.*, 6(4), 1031–1040, doi:10.5194/amt-6-1031-2013.

Colorado Department of Public Health and Environment (CDPHE) (2008), Denver metro area & north front range 8-hour ozone State Implementation Plan (SIP) Technical Support Documents (TSD), Appendix E, Executive Summary. [Available at http://www.colorado.gov/airquality/documents/deno308/.]

Colorado Department of Public Health and Environment (CDPHE) (2015), Ozone standard exceedance summary table. [Available at http://www.colorado.gov/airquality/html_resources/ozone_summary_table.pdf.] Colorado.gov.

Colorado Department of Public Health and Environment (CDPHE) (2016), Ozone information. [Available at https://www.colorado.gov/pacific/cdphe/ozone-information.]

Colorado Oil and Gas Conservation Commission (COGCC) (1/2016), Oil and natural gas wells data available in the "Downloads" section. [Available at http://cogcc.state.co.us/data2.html-/downloads.]

Colorado Oil and Gas Conservation Commission (COGCC) (2/2016), County level production available in the "DataBase" section. [Available at http://cogcc.state.co.us/.]

Cooper, O. R., R.-S. Gao, D. Tarasick, T. Leblanc, and C. Sweeney (2012), Long-term ozone trends at rural ozone monitoring sites across the United States, 1990–2010, *J. Geophys. Res.*, *117*, D22307, doi:10.1029/2012JD018261.

Cooper, O. R., A. O. Langford, D. D. Parrish, and D. W. Fahey (2015), Challenges of a lowered U.S. ozone standard, *Science*, *348*(6239), 1096–1097.

Crook, N. A., T. L. Clark, and M. W. Moncrieff (1990), The Denver Cyclone. Part I: Generation in low Froude number flow, *J. Atmos. Sci.*, *47*(23), 2725–2742, doi:10.1175/1520-0469(1990)047<2725:TDCPIG>2.0.CO;2.

Crosson, E. R. (2008), A cavity ring-down analyzer for measuring atmospheric levels of methane, carbon dioxide, and water vapor, *Appl. Phys. B*, *92*(3), 403–408, doi:10.1007/s00340-008-3135-y.

Crutzen, P. J. (1970), The influence of nitrogen oxides on the atmospheric ozone content, *Q. J. R. Meteorol. Soc.*, *96*(408), 320–325, doi:10.1002/qj.49709640815.

Duncan, B. N., L. N. Lamsal, A. M. Thompson, Y. Yoshida, Z. Lu, D. G. Streets, M. M. Hurwitz, and K. E. Pickering (2016), A space-based, high-resolution view of notable changes in urban NOx pollution around the world (2005–2014), *J. Geophys. Res. Atmos.*, *121*, 976–996, doi:10.1002/2015JD024121.

Edwards, P. M., et al. (2013), Ozone photochemistry in an oil and natural gas extraction region during winter: simulations of a snow-free season in the Uintah Basin, Utah, *Atmos. Chem. Phys.*, *13*(17), 8955–8971, doi:10.5194/acp-13-8955-2013.

Edwards, P. M., et al. (2014), High winter ozone pollution from carbonyl photolysis in an oil and gas basin, *Nature*, *514*(7522), 351–354, doi:10.1038/nature13767.

Emmerson, K. M., and M. J. Evans (2009), Comparison of tropospheric gas-phase chemistry schemes for use within global models, *Atmos. Chem. Phys.*, *9*(5), 1831–1845, doi:10.5194/acp-9-1831-2009.

Environmental Protection Agency (US EPA) (2016), National Emissions Inventory (NEI) air pollutant emissions trends data. [Available at https://www.epa.gov/air-emissions-inventories/air-pollutant-emissions-trends-data.]

Field, R. A., J. Soltis, M. C. McCarthy, S. Murphy, and D. C. Montague (2015), Influence of oil and gas field operations on spatial and temporal distributions of atmospheric non-methane hydrocarbons and their effect on ozone formation in winter, *Atmos. Chem. Phys.*, *15*(6), 3527–3542, doi:10.5194/acp-15-3527-2015.

Fuchs, H., W. P. Dube, B. M. Lerner, N. L. Wagner, E. J. Williams, and S. S. Brown (2009), A sensitive and versatile detector for atmospheric NO2 and NOx based on blue diode laser cavity ring-down spectroscopy, *Environ. Sci. Technol.*, *43*(20), 7831–7836, doi:10.1021/es902067h.

Gentner, D. R., et al. (2014), Emissions of organic carbon and methane from petroleum and dairy operations in California's San Joaquin Valley, *Atmos. Chem. Phys.*, *14*(10), 4955–4978, doi:10.5194/acp-14-4955-2014.

Gerbig, C., S. Schmitgen, D. Kley, A. Volz-Thomas, K. Dewey, and D. Haaks (1999), An improved fast-response vacuum-UV resonance fluorescence CO instrument, *J. Geophys. Res.*, *104*(D1), 1699–1704, doi:10.1029/1998JD100031.

Gilman, J. B., J. F. Burkhart, B. M. Lerner, E. J. Williams, and W. C. Kuster (2010), Ozone variability and halogen oxidation within the Arctic and sub-Arctic springtime boundary layer, *Atmos. Chem. Phys.*, *10*(21), 10,223–10,236.

Gilman, J. B., B. M. Lerner, W. C. Kuster, and J. A. de Gouw (2013), Source signature of volatile organic compounds from oil and natural gas operations in northeastern Colorado, *Environ. Sci. Technol.*, *47*(3), 1297–1305, doi:10.1021/es304119a.

Griffin, R. J., C. A. Johnson, R. W. Talbot, H. Mao, R. S. Russo, Y. Zhou, and B. C. Sive (2004), Quantification of ozone formation metrics at Thompson Farm during the New England Air Quality Study (NEAQS) 2002, *J. Geophys. Res.*, *109*, D24302, doi:10.1029/2004JD005344.

Harrison, L. L., J. Michalsky, and J. Berndt (1994), Automated multifilter rotating shadow-band radiometer: An instrument for optical depth and radiation measurements, *Appl. Opt.*, *33*(22), 5118–5125.

Helmig, D., C. R. Thompson, J. Evans, P. Boylan, J. Hueber, and J. H. Park (2014), Highly elevated atmospheric levels of volatile organic compounds in the Uintah Basin, Utah, *Environ. Sci. Technol.*, *48*(9), 4707–4715, doi:10.1021/es405046r.

Hirsch, A. I., J. W. Munger, D. J. Jacob, L. W. Horowitz, and A. H. Goldstein (1996), Seasonal variation of the ozone production efficiency per unit NOx at Harvard Forest, Massachusetts, *J. Geophys. Res.*, *101*(D7), 12,659–12,666, doi:10.1029/96JD00557.

Jenkin, M. E., J. C. Young, and A. R. Rickard (2015), The MCM v3.3.1 degradation scheme for isoprene, *Atmos. Chem. Phys.*, *15*(20), 11,433–11,459, doi:10.5194/acp-15-11433-2015.

Kaimal, J. C., and J. E. Gaynor (1983), The Boulder Atmospheric Observatory, *J. Climate Appl. Meteorol.*, *22*(5), 863–880.

Kemball-Cook, S., A. Bar-Ilan, J. Grant, L. Parker, J. Jung, W. Santamaria, J. Mathews, and G. Yarwood (2010), Ozone impacts of natural gas development in the Haynesville Shale, *Environ. Sci. Technol.*, *44*(24), 9357–9363, doi:10.1021/es1021137.

Kleinman, L., P. H. Daum, Y.-N. Lee, L. J. Nunnermacker, S. R. Springston, J. Weinstein-Lloyd, and J. Rudolph (2002), Ozone production efficiency in an urban area, *J. Geophys. Res.*, *107*(D23), 4733, doi:10.1029/2002JD002529.

Langford, A. O., et al. (2015), An overview of the 2013 Las Vegas Ozone Study (LVOS): Impact of stratospheric intrusions and long-range transport on surface air quality, *Atmos. Environ.*, *109*, 305–322, doi:10.1016/J.Atmosenv.2014.08.040.

Lin, X., M. Trainer, and S. C. Liu (1988), On the nonlinearity of the tropospheric ozone production, *J. Geophys. Res.*, *93*(D12), 15,879–15,888, doi:10.1029/JD093iD12p15879.

Madronich, S. S., R. L. McKenzie, L. O. Bjorn, and M. M. Caldwell (1998), Changes in biologically active ultraviolet radiation reaching the Earth's surface, *J. Photochem. Photobiol., B*, *46*(1–3), 5–19.

McManus, J. B., J. H. Shorter, D. D. Nelson, M. S. Zahniser, D. E. Glenn, and R. M. McGovern (2008), Pulsed quantum cascade laser instrument with compact design for rapid, high sensitivity measurements of trace gases in air, *Appl. Phys. B*, *92*(3), 387–392, doi:10.1007/s00340-008-3129-9.

Michalsky, J. J., and G. B. Hodges (2013), Field measured spectral albedo–Four years of data from the Western U.S. Prairie, *J. Geophys. Res. Atmos.*, *118*, 813–825, doi:10.1002/jgrd.50149.

Neuman, J. A., et al. (2009), Relationship between photochemical ozone production and NOx oxidation in Houston, Texas, *J. Geophys. Res.*, *114*, D00F08, doi:10.1029/2008JD011688.

Nunnermacker, L. J., et al. (1998), Characterization of the Nashville urban plume on July 3 and July 18, 1995, *J. Geophys. Res.*, *103*(D21), 28,129–28,148, doi:10.1029/98JD01961.

Olszyna, K. J., E. M. Bailey, R. Simonaitis, and J. F. Meagher (1994), O3 and NO y relationships at a rural site, *J. Geophys. Res.*, *99*(D7), 14,557–14,563, doi:10.1029/94JD00739.

Oltmans, S., R. Schnell, B. Johnson, G. Petron, T. Mefford, and R. Neely (2014), Anatomy of wintertime ozone associated with oil and natural gas extraction activity in Wyoming and Utah, *Elementa Sci. Anthropocene*, *2*, 000024, doi:10.12952/journal.elementa.000024.

Pacsi, A. P., Y. Kimura, G. McGaughey, E. C. McDonald-Buller, and D. T. Allen (2015), Regional ozone impacts of increased natural gas use in the Texas power sector and development in the Eagle Ford Shale, *Environ. Sci. Technol.*, *49*(6), 3966–3973, doi:10.1021/es5055012.

Peischl, J., et al. (2012), Airborne observations of methane emissions from rice cultivation in the Sacramento Valley of California, *J. Geophys. Res.*, *117*, D00V25, doi:10.1029/2012JD017994.

Pétron, G., et al. (2012), Hydrocarbon emissions characterization in the Colorado Front Range: A pilot study, *J. Geophys. Res.*, *117*, D04304, doi:10.1029/2011JD016360.

Pétron, G., et al. (2014), A new look at methane and non-methane hydrocarbon emissions from oil and natural gas operations in the Colorado Denver-Julesburg Basin, *J. Geophys. Res. Atmos.*, *119*, 6836–6852, doi:10.1002/2013JD021272.

Rappenglück, B., et al. (2014), Strong wintertime ozone events in the Upper Green River basin, Wyoming, *Atmos. Chem. Phys.*, *14*(10), 4909–4934, doi:10.5194/acp-14-4909-2014.

Rodriguez, M. A., M. G. Barna, and T. Moore (2009), Regional impacts of oil and gas development on ozone formation in the Western United States, *J. Air Waste Manage.*, *59*(9), 1111–1118, doi:10.3155/1047-3289.59.9.1111.

Roelofs, G.-J., and J. Lelieveld (1995), Distribution and budget of O_3 in the troposphere calculated with a chemistry general circulation model, *J. Geophys. Res.*, *100*(D10), 20,983–20,998, doi:10.1029/95JD02326.

Russell, A., J. Milford, M. S. Bergin, S. McBride, L. McNair, Y. Yang, W. R. Stockwell, and B. Croes (1995), Urban ozone control and atmospheric reactivity of organic gases, *Science*, *269*(5223), 491–495, doi:10.1126/science.269.5223.491.

Rutter, A. P., R. J. Griffin, B. K. Cevik, K. M. Shakya, L. Gong, S. Kim, J. H. Flynn, and B. L. Lefer (2015), Sources of air pollution in a region of oil and gas exploration downwind of a large city, *Atmos. Environ.*, *120*, 89–99, doi:10.1016/j.atmosenv.2015.08.073.

Ryerson, T. B., et al. (1998), Emissions lifetimes and ozone formation in power plant plumes, *J. Geophys. Res.*, *103*(D17), 22,569–22,583, doi:10.1029/98JD01620.

Schnell, R. C., S. J. Oltmans, R. R. Neely, M. S. Endres, J. V. Molenar, and A. B. White (2009), Rapid photochemical production of ozone at high concentrations in a rural site during winter, *Nat. Geosci.*, *2*(2), 120–122.

Shetter, R. E., et al. (2003), Photolysis frequency of NO2: Measurement and modeling during the International Photolysis Frequency Measurement and Modeling Intercomparison (IPMMI), *J. Geophys. Res.*, *108*(D16), 8544, doi:10.1029/2002JD002932.

Sillman, S., D. He, M. R. Pippin, P. H. Daum, D. G. Imre, L. I. Kleinman, J. H. Lee, and J. Weinstein-Lloyd (1998), Model correlations for ozone, reactive nitrogen, and peroxides for Nashville in comparison with measurements: Implications for O_3-NO x -hydrocarbon chemistry, *J. Geophys. Res.*, *103*(D17), 22,629–22,644, doi:10.1029/98JD00349.

St. John, J. C., W. L. Chameides, and R. Saylor (1998), Role of anthropogenic NO x and VOC as ozone precursors: A case study from the SOS Nashville/Middle Tennessee Ozone Study, *J. Geophys. Res.*, *103*(D17), 22,415–22,423, doi:10.1029/98JD00973.

Swarthout, R. F., R. S. Russo, Y. Zhou, A. H. Hart, and B. C. Sive (2013), Volatile organic compound distributions during the NACHTT campaign at the Boulder Atmospheric Observatory: Influence of urban and natural gas sources, *J. Geophys. Res. Atmos.*, *118*, 10,614–10,637, doi:10.1002/jgrd.50722.

Swarthout, R. F., R. S. Russo, Y. Zhou, B. M. Miller, B. Mitchell, E. Horsman, E. Lipsky, D. C. McCabe, E. Baum, and B. C. Sive (2015), Impact of Marcellus Shale natural gas development in southwest Pennsylvania on volatile organic compound emissions and regional air quality, *Environ. Sci. Technol.*, *49*(5), 3175–3184, doi:10.1021/es504315f.

Szoke, E. J. (1991), Eye of the Denver Cyclone, *Mon. Weather Rev.*, *119*(5), 1283–1292, doi:10.1175/1520-0493(1991)119<1283:EOTDC>2.0.CO;2.

Szoke, E. J., M. L. Weisman, J. M. Brown, F. Caracena, and T. W. Schlatter (1984), A subsynoptic analysis of the Denver tornadoes of 3 June 1981, *Mon. Weather Rev.*, *112*(4), 790–808, doi:10.1175/1520-0493(1984)112<0790:ASAOTD>2.0.CO;2.

Toth, J. J., and R. H. Johnson (1985), Summer surface flow characteristics over northeast Colorado, *Mon. Weather Rev.*, *113*(9), 1458–1469, doi:10.1175/1520-0493(1985)113<1458:SSFCON>2.0.CO;2.

Trainer, M., et al. (1993), Correlation of ozone with NOy in photochemically aged air, *J. Geophys. Res.*, *98*(D2), 2917–2925, doi:10.1029/92JD01910.

Trainer, M., B. A. Ridley, M. P. Buhr, G. Kok, J. Walega, G. Hübler, D. D. Parrish, and F. C. Fehsenfeld (1995), Regional ozone and urban plumes in the southeastern United States: Birmingham, A case study, *J. Geophys. Res.*, *100*(D9), 18,823–18,834, doi:10.1029/95JD01641.

United States Department of Agriculture (USDA) (2016), 2012 census of agriculture, county level data available from the USDA National Agricultural Statistics Service Quick Stats. [Available at http://quickstats.nass.usda.gov/.]

Washenfelder, R. A., N. L. Wagner, W. P. Dube, and S. S. Brown (2011a), Measurement of atmospheric ozone by cavity ring-down spectroscopy, *Environ. Sci. Technol.*, *45*(7), 2938–2944, doi:10.1021/es103340u.

Washenfelder, R. A., et al. (2011b), The glyoxal budget and its contribution to organic aerosol for Los Angeles, California, during CalNex 2010, *J. Geophys. Res.*, *116*, D00V02, doi:10.1029/2011JD016314.

Wilczak, J. M., and J. W. Glendening (1988), Observations and mixed-layer modeling of a terrain-induced mesoscale gyre: The Denver Cyclone, *Mon. Weather Rev.*, *116*(12), 2688–2711, doi:10.1175/1520-0493(1988)116<2688:OAMLMO>2.0.CO;2.

Wild, R. J., et al. (2014), A measurement of total reactive nitrogen, NOy, together with NO2, NO, and O_3 via cavity ring-down spectroscopy, *Environ. Sci. Technol.*, *48*(16), 9609–9615, doi:10.1021/es501896w.

Zaveri, R. A., C. M. Berkowitz, L. I. Kleinman, S. R. Springston, P. V. Doskey, W. A. Lonneman, and C. W. Spicer (2003), Ozone production efficiency and NOx depletion in an urban plume: Interpretation of field observations and implications for evaluating O_3-NOx-VOC sensitivity, *J. Geophys. Res.*, *108*(D14), 4436, doi:10.1029/2002JD003144.